



# Rejuvenating Classical Source Localization Methods with Spatial Graph Filters

Shihao Yang<sup>1</sup>, Meng Jiao<sup>1</sup>, Jing Xiang<sup>2</sup>, Daphne Kalkanis<sup>1</sup>, Hai Sun<sup>3</sup>,  
and Feng Liu<sup>1</sup>✉

<sup>1</sup> School of Systems and Enterprises, Stevens Institute of Technology,  
Hoboken, NJ 07030, USA

{syang57,mjiao,dkalkani,fliu22}@stevens.edu

<sup>2</sup> MEG Center, Division of Neurology, Cincinnati Children's Hospital Medical  
Center, Cincinnati, OH, USA

<sup>3</sup> Department of Neurosurgery, Rutgers Robert Wood Johnson Medical School,  
Brunswick, NJ, USA

**Abstract.** EEG/MEG source imaging (ESI) aims to find the underlying brain sources to explain the observed EEG or MEG measurement. Multiple classical approaches have been proposed to solve the ESI problem based on different neurophysiological assumptions. To support the clinical decision making, it is important to estimate not only the exact location of source signal but also the boundary of extended source activation. Traditional methods usually render over-diffuse or sparse solution, which limits the source extent estimation accuracy. In this work, we exploit the graph structure defined in the 3D mesh of the brain by decomposing the spatial graph signal into low-, medium-, and high-frequency sub-spaces, and leverage the low frequency components of graph Fourier basis to approximate the extended region of source activation. We integrate the classical source localization methods with the low frequency subspace components derived from the spatial graph signal. The proposed method can effectively reconstruct focal extent patterns and significantly improve the performance compared to classical algorithms through both synthetic data and real EEG data.

**Keywords:** EEG/MEG Source Imaging · Inverse Problem · Graph Signal Processing · Spatial Graph Filter

## 1 Introduction

EEG/MEG is a non-invasive measurement with high temporal and low spatial resolution, which collects signals on the scalp through electrodes for analysis of brain neural activity. At the same time, EEG/MEG is also a direct and real-time way to detect a spontaneous or induced activity of the brain [1]. EEG/MEG devices have the advantages of cost-effectiveness, portability, and versatility.

EEG, in particular, is widely recognized as a powerful tool for capturing real-time brain function by measuring neuronal processes [2]. The problem of EEG/MEG source localization can be further divided into two sub-problems, the forward and the inverse problem. The forward problem of EEG/MEG is to determine the surface potential or magnetic field strength of the scalp from a given configuration of neuronal current activity, whereas the inverse problem is defined as the reconstruction of brain activity sources from external electromagnetic signals which is also known as the EEG/MEG source imaging (ESI) problem [3]. However, the number of EEG/MEG external detection channels is far less than that of the brain sources, which makes the ESI an ill-posed problem.

In the past decades, numerous algorithms have been developed with different assumptions on the configuration of the source signal. One seminal work is minimum norm estimate (MNE) where  $\ell_2$  norm is used as a regularization [4], which is to explain the observed signal using a potential solution with the minimum energy. Different variants of the MNE algorithm include dynamic statistical parametric mapping (dSPM) [5] and standardized low-resolution brain electromagnetic tomography (sLORETA) [6]. The  $\ell_2$ -norm based methods tend to render spatially diffuse source estimation. To promote a sparse solution, Uutela *et al.* [7] introduced the  $\ell_1$ -norm, known as minimum current estimate (MCE). Also, Rao and Kreutz-Delgado proposed an affine scaling method [8] for a sparse ESI solution. The focal underdetermined system solution (FOCUSS) proposed by Gorodnitsky *et al.* encourages a sparse solution by introducing the  $\ell_p$ -norm regularization [9]. Besides, Bore *et al.* also proposed to use the  $\ell_p$ -norm regularization ( $p < 1$ ) on the source signal and the  $\ell_1$  norm on the data fitting error term [10]. Babadi *et al.* [11] demonstrated that sparsely distributed solutions to event-related stimuli could be found using a greedy subspace-pursuit algorithm. Wipf *et al.* proposed a unified Bayesian learning method [12] that can automatically calculate the hyperparameters for the inverse problems under an empirical Bayesian framework and the sparsity of the solution is also guaranteed. It is worth noting that the sparse constraint can be applied to the original source signal or the transformed spatial gradient domain [13–16]. As the brain sources are not activated discretely due to the conductor property, an extended area of source estimation is preferred [17], and it has been used for multiple applications, such as somatosensory cortical mapping [18], and epileptogenic zone in focal epilepsy patients [19].

Following the early work of applying GSP to the ESI problem [20,21], in this work, we proposed to use GSP and incorporate the low frequency spatial representation for the source space and rejuvenate the classical ESI methods for the estimation of an extended area of source activation, and illustrate the importance of using GSP for an extended area of source activation.

## 2 Method

In this section, we start by introducing the ESI inverse problem, followed by the presentation of the graph Fourier transform (GFT). Then, we propose a improve the classical source localization methods using the low-pass spatial graph filters.

### 2.1 EEG/MEG Source Imaging Problem

The source imaging forward problem can be described as the format  $Y = KS + E$ , where  $Y \in \mathbb{R}^{C \times T}$  is the EEG/MEG measurements from the scalp,  $C$  is the number of EEG/MEG channels,  $T$  is the time sequence length,  $K \in \mathbb{R}^{C \times N}$  is the *leadfield* matrix which performs a linear mapping from the brain sources to the EEG/MEG electrodes on the scalp,  $N$  is the number of source locations,  $S \in \mathbb{R}^{N \times T}$  represents the active source amplitudes in  $N$  source locations for all the  $T$  time points, and  $E$  is the noise which can be assumed to follow the Gaussian distribution with zero mean and identity covariance. The inverse problem is to estimate  $S$  given  $Y$  and  $K$ . Since the source number  $N$  is much larger than the electrode number  $C$ , which makes the inverse problem ill-posed, it is challenging to obtain a unique and stable solution. Thus, in order to constrain the solution space, various regularization terms were designed based on the prior assumption of the source structure. In this case, the inverse problem can be formulated as below:

$$S = \operatorname{argmin}_S \frac{1}{2} \|Y - KS\|_F^2 + \lambda R(S), \quad (1)$$

where  $\|\cdot\|_F$  is the Frobenius norm, and  $S$  can be obtained by solving the minimizing problem. The first term in Eq. (1) is *datafitting* trying to explain the recorded EEG measurements. The second term is called the *regularization* term, which is imposed to find a unique solution by using sparsity or other neurophysiology inspired regularization. For example, if  $R(S)$  equals  $\ell_2$  norm, the problem is called minimum norm estimate (MNE).

### 2.2 Graph Fourier Transform (GFT)

Consider an undirected graph  $G = \{\mathcal{V}, A\}$  generated from the 3D mesh of cortex, where  $\mathcal{V} = \{v_1, v_2, \dots, v_N\}$  is the set of  $N$  nodes,  $A$  is the weighted adjacent matrix with entries given by the edge weights  $a_{ij}$  that represents the connection strength between node  $i$  and node  $j$ . The graph Laplacian matrix is defined as  $L = D - A$ , where  $D$  is the in-degree matrix with  $D_{ii} = \sum_{j \neq i} A_{ij}$ . Since  $L$  is a positive semi-definite matrix, its eigenvalues are all greater or equal to 0 which are usually taken as the frequency of GFT, and the associated eigenvectors  $U = [u_1, u_2, \dots, u_N]$ ,  $U \in \mathbb{R}^{N \times N}$  can be regarded as the basis signals of GFT where any signal in the graph can be approximated as the linear combinations of basis. Thus, the graph Fourier transform for a signal  $S$  can be defined as  $\tilde{S} = U^T S$ , whereas the inverse graph Fourier transform is given as  $S = U \tilde{S}$ . Then we define normalized graph frequency (NGF) as

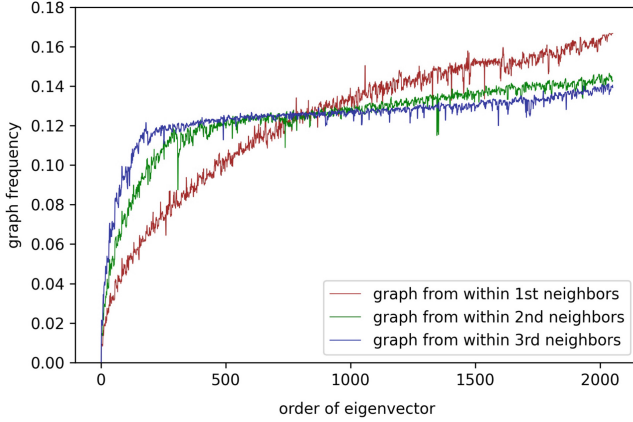


**Fig. 1.** Graph frequency of the eigenvectors.

$$f_G(u_i) = \frac{f_s(u_i)}{Tr(L)}, \tag{2}$$

where  $Tr(L)$  is the trace of  $L$ , and  $f_s(u_i)$  is defined as

$$f_s(u_i) = \sum_{m=1}^N \sum_{n \in \mathcal{N}(m)} \mathbb{I}(u_i(m)u_i(n) < 0)/2, \tag{3}$$

where  $\mathcal{N}(m)$  represents all neighbors of node  $m$ , and  $\mathbb{I}(\cdot)$  is the indicator function which equals 1 if the values of  $u_i$  on node  $m$  and  $n$  have different sign and 0 otherwise. The number of sign flip at time  $t$  indicate how many zero crossing of a basis signal within a bounded region at  $t$ .

We calculated the NGF in the whole time series within first-order neighbors, second-order neighbors, and third-order neighbors respectively. The spectrogram, which is illustrated in Fig. 1, reveals that the NGF is positively correlated with the size of the eigenvalue of  $L$ . Thus we can further separate  $U$  into low, medium, and high-frequency components according to NGF values, and reformat it as  $U = [U_L, U_M, U_H]$ .

### 2.3 Inverse Problem with Spatial Graph Filters

The existing source localization methods can be distracted by the high-frequency components and result in a spread-out solution while reconstructing the focal extend area, even the  $\ell_1$ -norm and  $\ell_{2,1}$ -norm based method that is designed to promote the sparsity can hardly give a satisfying reconstruction result. Moreover, they do not take source spatial frequency correlation into consideration. The proposed method is trying to rejuvenate classical source localization methods using spatial graph filters by keeping the spatially low- and the top part of

medium-frequency components  $[U_L, \tilde{U}_M] \in \mathbb{R}^{N \times P}$  as a spatial graph filter to reconstruct the focally extended sources, where  $P$  is the number of frequency components preserved for reconstruction. Here we replace the  $S$  in Eq. (1) with  $\tilde{U}\tilde{S}^*$  for dimensionality reduction in  $S$  and  $K$ , where  $\tilde{U} = [U_L, \tilde{U}_M]$ , and  $\tilde{S}^* \in \mathbb{R}^{P \times T}$  is the estimated source signal with dimensionality reduction that contains smooth part of the original signal, in other words, the part of source extents. Then we can transform Eq. (1) to the problem of estimating  $\tilde{S}^*$  by introducing the spatial graph filter with the form as below

$$\tilde{S}^* = \underset{\tilde{S}^*}{\operatorname{argmin}} \frac{1}{2} \|Y - K\tilde{U}\tilde{S}^*\|_F^2 + \lambda R(\tilde{S}^*), \quad (4)$$

Finally,  $S$  can be simply obtained from  $\tilde{U}\tilde{S}^*$ . The intuition is that the main energy of the source signal usually lies in the low-frequency components which are associated with the regions on the cortex with relatively large source extend area in a time series. Keeping the low graph frequency could promote a source extend area reconstruction and decrease the impact of the noise. Moreover, the reduced dimensional estimation in the inverse problem could further constrain the solution space and make the solution more easily solved and robust.

### 3 Numerical Experiments

In this section, we conducted numerical experiments to validate the effectiveness of the proposed method on synthetic EEG data under different levels of neighbors (LNs), Signal Noise Ratio (SNR) settings and further validate it on real MEG recordings from a visual-auditory test.

#### 3.1 Simulation Experiments

We first conducted experiments on synthetic data with known activation patterns.

**Forward Model:** To generate synthetic EEG data, we used a real head model to compute the leadfield matrix. The T1-MRI images were scanned from a 26-year-old male subject. The brain tissue segmentation and source surface reconstruction were conducted using FreeSurfer [22]. Then a three-layer boundary element method (BEM) head was built based on these surfaces. A 128-channel BioSemi EEG cap layout was used and the EEG channels were co-registered with the head model using Brainstorm and then further validated on the MNE-Python toolbox [23]. The source space contains 1026 sources in each hemisphere, with 2052 sources combined, resulting in a leadfield matrix  $L$  with a dimension of 128 by 2052 (Fig. 2).

**Synthetic Data Generation:** To make the synthetic data more realistic, 200 out of 2052 locations in the source space were activated. Furthermore, as illustrated in Fig. 3, we used 3 different neighborhood levels (1-, 2-, and 3-level of the

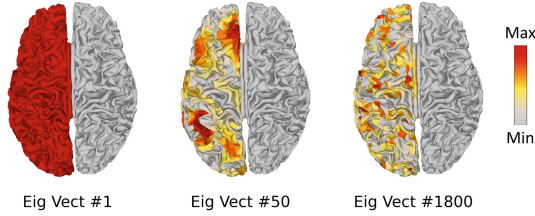


**Fig. 2.** Source distributions corresponding to eigenvectors with different NGFs.

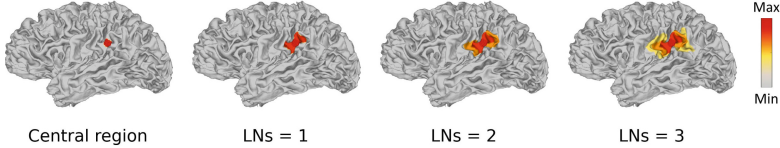


**Fig. 3.** Brain source distributions with different levels of neighbors (LNs).

neighborhood) to represent different sizes of source extents, then we activated the whole “patch” with different neighborhood levels at the same time. The activation strength of the 1-, 2-, and 3-level adjacent regions was successively set to be 80%, 60%, and 40% of the central region. The strength of the source signal was set to be constant, then the scalp EEG data was calculated based on the forward model under different SNR settings (SNR = 40 dB, 30 dB, 20 dB, and 10 db). SNR is defined as the ratio of the signal power  $P_{\text{signal}}$  to the noise power  $P_{\text{noise}}$ :  $\text{SNR} = 10 \log(P_{\text{signal}}/P_{\text{noise}})$ .

In total, there were 12: 3 (source extents)  $\times$  4 (SNRs) data sets ( $Y$  and  $S$  pairs).

**Experimental Settings:** We adopted MNE [4], MCE [7],  $\ell_{2,1}$ (MxNE) [24], dSPM [5], and sLORETA [6], as benchmark algorithms for comparison. We separately performed EEG source localization based on benchmark algorithms with and without the proposed GFT-based dimensionality reduction method. Next, we performed brain source reconstruction on the results from all algorithms. All the experiments were conducted on Linux environment with CPU Intel(R) Xeon(R) Gold 6130 CPU @2.10 GHz and 128 GB memory. The performance of each algorithm was quantitatively evaluated based on the following metrics:

- (1) *Localization error (LE)*: it measures the Euclidean distance between centers of two source locations on the cortex meshes.
- (2) *Area under curve (AUC)*: it is particularly useful to characterize the overlap of an extended source activation pattern.

Better performance for localization is expected if LE is close to 0 and AUC is close to 1. The performance comparison between the proposed method and benchmark algorithms on LE and AUC is summarized in Table 1, and the boxplot figures for SNR = 40 dB, and 20 dB are given in Fig. 4. The comparison between

**Table 1.** Performance Evaluation

SNR	Method	Source with LNs = 1		Source with LNs = 2		Source with LNs = 3	
		LE (std)	AUC (std)	LE (std)	AUC (std)	LE (std)	AUC (std)
40 dB	MCE	15.028 ± 11.465	0.595 ± 0.064	15.286 ± 10.474	0.568 ± 0.031	18.656 ± 12.154	0.548 ± 0.017
	L21	16.114 ± 10.433	0.631 ± 0.096	14.993 ± 9.121	0.627 ± 0.054	15.237 ± 8.400	0.625 ± 0.052
	MNE	9.828 ± 6.455	0.992 ± 0.014	10.294 ± 6.750	0.977 ± 0.019	11.216 ± 7.452	0.961 ± 0.018
	sLORETA	7.349 ± 6.530	0.988 ± 0.018	11.504 ± 9.868	0.963 ± 0.026	15.567 ± 11.607	0.935 ± 0.025
	dSPM	33.666 ± 22.034	0.970 ± 0.027	39.868 ± 22.844	0.927 ± 0.039	47.382 ± 23.449	0.883 ± 0.043
	GFT-MCE	25.969 ± 22.269	0.975 ± 0.046	16.411 ± 14.091	0.988 ± 0.017	13.547 ± 9.922	0.983 ± 0.026
	GFT-L21	9.814 ± 7.416	0.996 ± 0.018	5.144 ± 6.607	0.999 ± 0.004	4.054 ± 6.130	0.998 ± 0.010
	GFT-MNE	3.812 ± 5.028	0.999 ± 0.001	6.526 ± 6.059	0.983 ± 0.020	7.689 ± 5.879	0.958 ± 0.023
	GFT-sLORETA	4.992 ± 6.440	0.996 ± 0.016	7.424 ± 6.144	0.971 ± 0.026	8.803 ± 6.553	0.947 ± 0.028
	GFT-dSPM	3.625 ± 5.346	0.999 ± 0.006	5.898 ± 5.374	0.992 ± 0.013	7.654 ± 6.093	0.968 ± 0.027
30 dB	MCE	14.917 ± 11.426	0.595 ± 0.065	14.779 ± 9.607	0.568 ± 0.030	18.324 ± 11.870	0.548 ± 0.017
	L21	16.460 ± 12.235	0.630 ± 0.096	14.690 ± 9.188	0.625 ± 0.053	15.330 ± 8.825	0.620 ± 0.051
	MNE	9.340 ± 6.446	0.983 ± 0.027	9.806 ± 6.493	0.958 ± 0.026	9.878 ± 6.676	0.926 ± 0.025
	sLORETA	6.358 ± 5.896	0.980 ± 0.035	8.670 ± 7.365	0.944 ± 0.036	12.347 ± 9.650	0.899 ± 0.033
	dSPM	31.885 ± 21.226	0.961 ± 0.044	36.423 ± 21.313	0.904 ± 0.053	42.922 ± 22.799	0.841 ± 0.055
	GFT-MCE	25.787 ± 22.258	0.975 ± 0.046	15.633 ± 12.640	0.989 ± 0.017	13.507 ± 9.875	0.983 ± 0.027
	GFT-L21	9.603 ± 7.393	0.996 ± 0.017	5.084 ± 6.564	0.999 ± 0.004	3.963 ± 5.874	0.998 ± 0.010
	GFT-MNE	3.236 ± 4.663	0.999 ± 0.003	5.357 ± 5.308	0.970 ± 0.030	6.921 ± 6.426	0.920 ± 0.034
	GFT-sLORETA	4.515 ± 5.990	0.994 ± 0.018	6.752 ± 6.264	0.949 ± 0.034	7.522 ± 6.589	0.902 ± 0.034
	GFT-dSPM	2.888 ± 4.292	0.999 ± 0.002	4.900 ± 5.316	0.985 ± 0.021	6.362 ± 5.907	0.946 ± 0.034
20 dB	MCE	14.655 ± 10.959	0.595 ± 0.064	14.353 ± 9.431	0.567 ± 0.031	18.302 ± 12.155	0.548 ± 0.017
	L21	16.309 ± 12.373	0.626 ± 0.099	14.087 ± 8.921	0.623 ± 0.052	16.213 ± 9.371	0.616 ± 0.044
	MNE	11.894 ± 14.620	0.951 ± 0.036	17.515 ± 23.602	0.897 ± 0.038	33.240 ± 37.552	0.846 ± 0.033
	sLORETA	7.237 ± 6.801	0.952 ± 0.051	10.639 ± 10.168	0.879 ± 0.056	19.948 ± 22.829	0.815 ± 0.043
	dSPM	27.257 ± 17.682	0.923 ± 0.070	34.975 ± 20.713	0.824 ± 0.082	41.651 ± 24.331	0.745 ± 0.074
	GFT-MCE	26.018 ± 22.997	0.976 ± 0.045	15.502 ± 12.445	0.989 ± 0.016	13.952 ± 13.063	0.983 ± 0.028
	GFT-L21	9.333 ± 7.512	0.996 ± 0.017	5.156 ± 6.540	0.999 ± 0.003	4.514 ± 6.281	0.998 ± 0.007
	GFT-MNE	3.840 ± 5.439	0.992 ± 0.019	5.630 ± 7.294	0.905 ± 0.049	10.217 ± 9.890	0.829 ± 0.042
	GFT-sLORETA	4.509 ± 6.420	0.979 ± 0.040	7.514 ± 9.787	0.873 ± 0.051	12.362 ± 12.321	0.803 ± 0.042
	GFT-dSPM	3.608 ± 4.907	0.996 ± 0.015	5.605 ± 7.311	0.941 ± 0.043	9.370 ± 8.110	0.864 ± 0.054
10 dB	MCE	15.526 ± 12.210	0.595 ± 0.061	14.247 ± 8.628	0.565 ± 0.029	17.944 ± 11.812	0.547 ± 0.017
	L21	16.434 ± 12.503	0.613 ± 0.090	15.248 ± 9.681	0.589 ± 0.051	16.307 ± 10.712	0.577 ± 0.038
	MNE	50.433 ± 47.357	0.871 ± 0.064	59.498 ± 48.871	0.804 ± 0.059	58.400 ± 46.174	0.766 ± 0.060
	sLORETA	47.815 ± 49.262	0.856 ± 0.087	59.048 ± 49.597	0.760 ± 0.082	57.989 ± 43.289	0.715 ± 0.079
	dSPM	31.356 ± 27.881	0.807 ± 0.112	37.304 ± 26.798	0.688 ± 0.101	41.865 ± 25.344	0.640 ± 0.089
	GFT-MCE	23.504 ± 16.491	0.975 ± 0.043	17.195 ± 13.654	0.988 ± 0.019	14.482 ± 11.684	0.982 ± 0.027
	GFT-L21	9.406 ± 8.054	0.996 ± 0.017	5.334 ± 5.735	0.998 ± 0.003	7.586 ± 6.490	0.948 ± 0.038
	GFT-MNE	21.581 ± 29.679	0.919 ± 0.077	28.806 ± 30.421	0.801 ± 0.067	39.258 ± 32.820	0.744 ± 0.066
	GFT-sLORETA	24.439 ± 30.874	0.891 ± 0.087	32.387 ± 31.514	0.771 ± 0.078	41.389 ± 36.626	0.729 ± 0.071
	GFT-dSPM	18.462 ± 25.356	0.937 ± 0.069	27.152 ± 30.759	0.818 ± 0.070	35.293 ± 30.785	0.750 ± 0.065

the reconstructed source distributions with a 3-level of the neighborhood and 40 dB SNR is shown in Fig. 5.

From Table 1 and Fig. 4 and 5, we can find that:

- (1) MNE, MCE,  $\ell_{2,1}$ , sLORETA, and dSPM can only reconstruct the brain sources when the activated area is small and the SNR level is high, and even the evaluation metrics are good in this case, the reconstruction for source extend area is poor as shown in Fig. 5. As the source range expands and the SNR decreases, a significant increase in LE and an obvious reduction in AUC can be observed. The reconstructed source distributions are no longer concentrated.
- (2) By contrast, the results of the rejuvenated methods outperform benchmark methods in most cases after applying the spatial graph filters. They both show good stability for varied neighborhood levels and SNR settings. Particularly, the performance of rejuvenated  $\ell_1$  regularization family (i.e.,  $\ell_1$ -norm

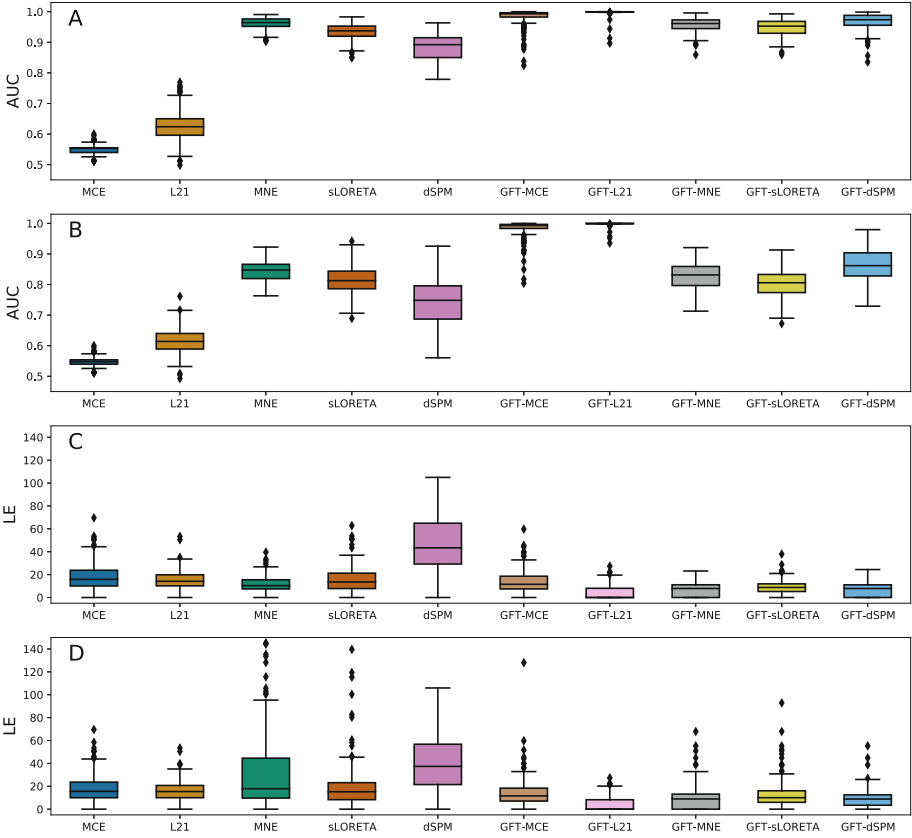


**Fig. 4.** Performance comparison of different algorithms on AUC and LE with 3-level of the neighborhood for SNR = 40 dB (subplot A and C), and SNR = 20 dB (subplot B and D).

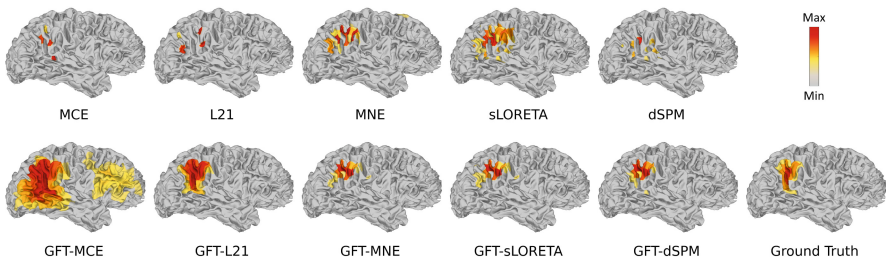


**Fig. 5.** Brain sources reconstruction by different ESI algorithms with the single activated area and 3-level of the neighborhood for SNR = 40 dB.



and  $\ell_{2,1}$ -norm) exhibits better performance on reconstructing source extents without losing its advantage in sparse focal source reconstruction and outperforms other methods in most instances.

### 3.2 Real Data Experiments

We further validated the proposed methodology on a real dataset that is publicly accessible through the MNE-Python package [23]. In this dataset acquisition, checkerboard patterns were presented into the left and right visual field, interspersed by tones to the left or right ear with stimuli interval 750 ms. The subject was asked to press a key with the right index finger as soon as possible after the appearance of a smiley face was presented at the center of the visual field [25]. Interictal spikes were extracted from the MEG measurements, and then we averaged these spikes for source reconstruction under MNE, MCE,  $\ell_{2,1}$ , dSPM, sLORETA with and without the proposed GFT-based dimensionality reduction method. The averaged spikes are shown in Fig. 6, and the reconstructed source distributions are shown in Fig. 7.

From Fig. 7, we can see that the source area estimated by MNE, MCE,  $\ell_{2,1}$ , sLORETA, and dSPM is highly broad. By contrast, and the rejuvenated methods provide more sparse focal source reconstructions. Moreover, the reconstructed focal for the rejuvenated methods falls primarily on areas with the strongest source signal, while others would spread to several regions. Obviously, the spatial graph filter in the rejuvenated methods promotes a concentrated and accurate estimation of the visual zone.

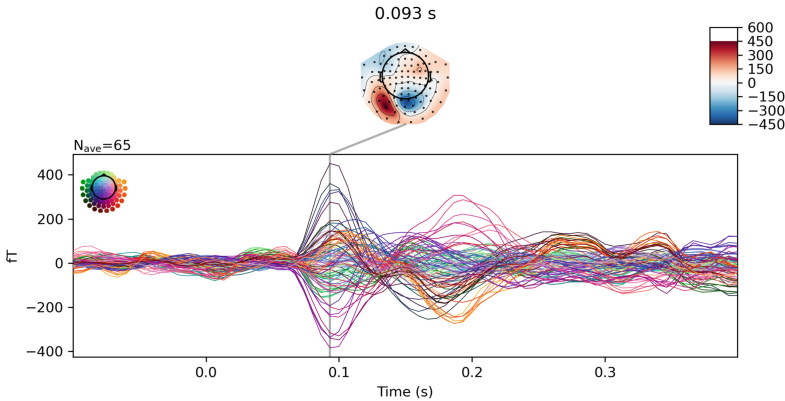


**Fig. 6.** Averaged MEG time series plot and topographies.

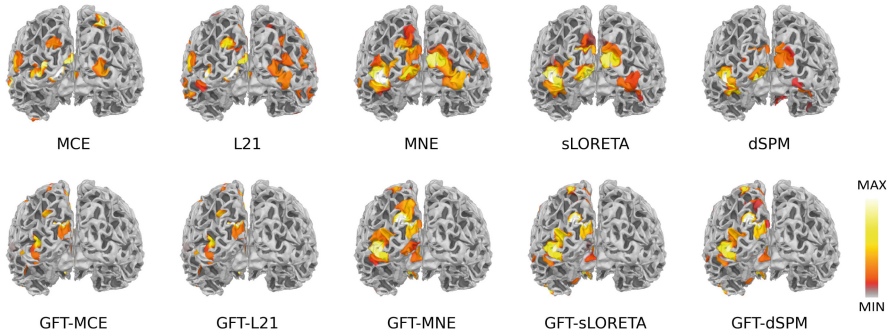


**Fig. 7.** Reconstructed source activation patterns from MEG data.

## 4 Conclusion

In this study, we rejuvenated classical source localization methods using spatial graph filters to solve the inverse problem of ESI. The proposed methodology enjoys the advantage of reconstructing focal source extents with sparsity and minimizing the impact from the noise by transforming the estimation of the source signal into an estimation of a lower dimensional latent variable in the subspace spanned by spatial frequency graph filters. Numerical experiments demonstrated that the proposed method performs particularly well on source extents, yields excellent robustness when the SNR level is low, and greatly improves the performance of the  $\ell_1$  family regularization. In the experiment on real data we performed, the proposed methodology provides a satisfactory reconstruction with more concentrated source distribution and more stability to noise than benchmark algorithms.

## References

1. Wendel, K., et al.: EEG/MEG source imaging: methods, challenges, and open issues. *Comput. Intell. Neurosci.* **2009** (2009)
2. Michel, C.M., Brunet, D.: EEG source imaging: a practical review of the analysis steps. *Front. Neurol.* **10**, 325 (2019)
3. Huang, G., et al.: Electromagnetic source imaging via a data-synthesis-based convolutional encoder-decoder network. *IEEE Trans. Neural Netw. Learn. Syst.* (2022)
4. Hämäläinen, M.S., Ilmoniemi, R.J.: Interpreting magnetic fields of the brain: minimum norm estimates. *Med. Biol. Eng. Comput.* **32**(1), 35–42 (1994). <https://doi.org/10.1007/BF02512476>
5. Dale, A.M., et al.: Dynamic statistical parametric mapping: combining fMRI and MEG for high-resolution imaging of cortical activity. *Neuron* **26**(1), 55–67 (2000)
6. Pascual-Marqui, R.D., et al.: Standardized low-resolution brain electromagnetic tomography (sLORETA): technical details. *Methods Find. Exp. Clin. Pharmacol.* **24**(Suppl D), 5–12 (2002)
7. Uutela, K., Hämäläinen, M., Somersalo, E.: Visualization of magnetoencephalographic data using minimum current estimates. *Neuroimage* **10**(2), 173–180 (1999)

8. Rao, B.D., Kreutz-Delgado, K.: An affine scaling methodology for best basis selection. *IEEE Trans. Sig. Process.* **47**(1), 187–200 (1999)
9. Gorodnitsky, I.F., George, J.S., Rao, B.D.: Neuromagnetic source imaging with FOCUSS: a recursive weighted minimum norm algorithm. *Electroencephalogr. Clin. Neurophysiol.* **95**(4), 231–251 (1995)
10. Bore, J.C., et al.: Sparse EEG source localization using LAPPS: least absolute l-P ( $0 < p < 1$ ) penalized solution. *IEEE Trans. Biomed. Eng.* **66**(7), 1927–1939 (2018)
11. Babadi, B., Obregon-Henao, G., Lamus, C., Hämäläinen, M.S., Brown, E.N., Purdon, P.L.: A subspace pursuit-based iterative greedy hierarchical solution to the neuromagnetic inverse problem. *Neuroimage* **87**, 427–443 (2014)
12. Wipf, D., Nagarajan, S.: A unified Bayesian framework for MEG/EEG source imaging. *Neuroimage* **44**(3), 947–966 (2009)
13. Ding, L., He, B.: Sparse source imaging in electroencephalography with accurate field modeling. *Hum. Brain Mapp.* **29**(9), 1053–1067 (2008)
14. Sohrabpour, A., Ye, S., et al.: Noninvasive electromagnetic source imaging and granger causality analysis: an electrophysiological connectome (eConnectome) approach. *IEEE Trans. Biomed. Eng.* **63**(12), 2474–2487 (2016)
15. Qin, J., Liu, F., Wang, S., Rosenberger, J.: EEG source imaging based on spatial and temporal graph structures. In: *International Conference on Image Processing Theory, Tools and Applications* (2017)
16. Liu, F., Wang, L., Lou, Y., Li, R.-C., Purdon, P.L.: Probabilistic structure learning for EEG/MEG source imaging with hierarchical graph priors. *IEEE Trans. Med. Imaging* **40**(1), 321–334 (2020)
17. Baillet, S., Mosher, J.C., Leahy, R.M.: Electromagnetic brain mapping. *IEEE Sig. Process. Mag.* **18**(6), 14–30 (2001)
18. Cai, C., Diwakar, M., Chen, D., Sekihara, K., Nagarajan, S.S.: Robust empirical Bayesian reconstruction of distributed sources for electromagnetic brain imaging. *IEEE Trans. Med. Imaging* **39**(3), 567–577 (2019)
19. Becker, H., et al.: EEG extended source localization: tensor-based vs. conventional methods. *Neuroimage* **96**, 143–157 (2014)
20. Liu, F., Wan, G., Semenov, Y.R., Purdon, P.L.: Extended electrophysiological source imaging with spatial graph filters. In: Wang, L., Dou, Q., Fletcher, P.T., Speidel, S., Li, S. (eds.) *MICCAI 2022*. LNCS, vol. 13431, pp. 99–109. Springer, Cham (2022). [https://doi.org/10.1007/978-3-031-16431-6\\_10](https://doi.org/10.1007/978-3-031-16431-6_10)
21. M. Jiao, et al.: A graph Fourier transform based bidirectional LSTM neural network for EEG source imaging. *Front. Neurosci.* **447** (2022)
22. Fischl, B.: FreeSurfer. *Neuroimage* **62**(2), 774–781 (2012)
23. Gramfort, A., et al.: MNE software for processing MEG and EEG data. *Neuroimage* **86**, 446–460 (2014)
24. Gramfort, A., Kowalski, M., Hämäläinen, M.: Mixed-norm estimates for the M/EEG inverse problem using accelerated gradient methods. *Phys. Med. Biol.* **57**(7), 1937 (2012)
25. Gramfort, A., Strohmeier, D., Haueisen, J., Hämäläinen, M.S., Kowalski, M.: Time-frequency mixed-norm estimates: sparse M/EEG imaging with non-stationary source activations. *Neuroimage* **70**, 410–422 (2013)